



## RESEARCH ARTICLE

10.1002/2016EA000172

## Key Points:

- Synchrotron X-ray fluorescence spectroscopy maps salts in sea ice
- Bromine concentration in brine inclusions is ten times the bulk concentration

## Correspondence to:

R. W. Obbard,  
Rachel.W.Obbard@Dartmouth.edu

## Citation:

Obbard, R. W., R. M. Lieb-Lappen, K. V. Nordick, E. J. Golden, J. R. Leonard, A. Lanzirotti, and M. G. Newville (2016), Synchrotron X-ray fluorescence spectroscopy of salts in natural sea ice, *Earth and Space Science*, 3, doi:10.1002/2016EA000172.

Received 22 MAR 2016

Accepted 14 OCT 2016

Accepted article online 23 OCT 2016

## Synchrotron X-ray fluorescence spectroscopy of salts in natural sea ice

Rachel W. Obbard<sup>1</sup>, Ross M. Lieb-Lappen<sup>1</sup>, Katherine V. Nordick<sup>1</sup>, Ellyn J. Golden<sup>1</sup>, Jeremiah R. Leonard<sup>2</sup>, Antonio Lanzirotti<sup>3</sup>, and Mathew G. Newville<sup>3</sup>

<sup>1</sup>Thayer School of Engineering, Dartmouth College, Hanover, New Hampshire, USA, <sup>2</sup>Worcester Polytechnic Institute, Worcester, Massachusetts, USA, <sup>3</sup>Center for Advanced Radiation Sources, University of Chicago, Chicago, Illinois, USA

**Abstract** We describe the use of synchrotron-based X-ray fluorescence spectroscopy to examine the microstructural location of specific elements, primarily salts, in sea ice. This work was part of an investigation of the location of bromine in the sea ice-snowpack-blowing snow system, where it plays a part in the heterogeneous chemistry that contributes to tropospheric ozone depletion episodes. We analyzed samples at beamline 13-ID-E of the Advanced Photon Source at Argonne National Laboratory. Using an 18 keV incident energy beam, we produced elemental maps of salts for sea ice samples from the Ross Sea, Antarctica. The distribution of salts in sea ice depends on ice type. In our columnar ice samples, Br was located in parallel lines spaced roughly 0.5 mm apart, corresponding to the spacing of lamellae in the skeletal region during initial ice growth. The maps revealed concentrations of Br in linear features in samples from all but the topmost and bottommost depths. For those samples, the maps revealed rounded features. Calibration of the Br elemental maps showed bulk concentrations to be 5–10 g/m<sup>3</sup>, with concentrations ten times larger in the linear features. Through comparison with horizontal thin sections, we could verify that these linear features were brine sheets or layers.

### 1. Introduction

Sea ice plays many roles in the polar regions, among them an insulating yet permeable layer between the ocean and atmosphere, a thermal reservoir for latent heat associated with freezing and melting, and a home for a microbial community [Martin *et al.*, 2011]. The physical and chemical processes in sea ice and their accurate representation in regional sea ice and climate models are important to a wide range of problems across disciplines. Sea ice's complexity arises from how it is formed and from the fact that it is multiphase—containing ice, liquid brine, solid precipitates, and gas—and heterogeneous in both structure and chemistry in three physical dimensions, as well as in time and temperature [Eicken, 1992, 1998; Petrich and Eicken, 2009]. Bulk properties such as electrical conductivity, chemical transport to the atmosphere, and brine drainage to the ocean below depend on microstructure and microchemistry and specifically the location and connectivity of salt water brine inclusions.

Bromine is one of the minor constituents of sea salt and brine. Its concentration is hundreds of times smaller than chlorine, but it plays a disproportionately important role in atmospheric chemistry. Bromine is a far more efficient catalyst of tropospheric ozone loss than chlorine, and bromine compounds are the trigger for the ozone depletion events that take place in the boundary layer atmosphere in polar springtime [Barrie *et al.*, 1988; Kreher *et al.*, 1997; Wessel *et al.*, 1998; Roscoe *et al.*, 2001; Frieß *et al.*, 2004]. The reaction originates from Br<sup>-</sup> ions in sea salt [Tang and McConnell, 1996], and reactive bromine compounds in the gas phase (BrO) multiply rapidly once the process has begun [e.g., Vogt *et al.*, 1996], producing the so-called “bromine explosion.” This is a heterogeneous reaction in that it requires the gas phase to come into contact with a condensed phase. Atmospheric chemists have sought for some time to identify the mechanism by which the bromide ion is made available for these reactions and specifically whether they were taking place primarily on the sea ice, on frost flowers, or on snow.

Sea water begins to freeze at  $-1.9^{\circ}\text{C}$ , and solute rejection during freezing produces relatively freshwater ice (5 practical salinity unit (psu)) with very salty liquid (up to 100 psu) concentrated in brine channels, as well as on both the surface of sea ice and at the ice-ocean interface [Thomas and Dieckmann, 2009]. As the system is cooled, the brine becomes more concentrated and solid salts begin to precipitate when solubility limits are reached. These include mirabilite ( $\text{Na}_2\text{SO}_4 \cdot 10\text{H}_2\text{O}$ ,  $-8.2^{\circ}\text{C}$ ), hydrohalite ( $\text{NaCl} \cdot 2\text{H}_2\text{O}$ ,  $-22.9^{\circ}\text{C}$ ), gypsum

©2016. The Authors.

This is an open access article under the terms of the Creative Commons Attribution-NonCommercial-NoDerivs License, which permits use and distribution in any medium, provided the original work is properly cited, the use is non-commercial and no modifications or adaptations are made.

( $\text{Ca}_2\text{SO}_4 \cdot 2\text{H}_2\text{O}$ ,  $-22.2^\circ\text{C}$ ), and magnesium chloride ( $\text{MgCl}_2$ ,  $-36.2^\circ\text{C}$ ) [Marion *et al.*, 1999]. In a single season, 1–2 m of sea ice typically forms in the polar regions. It is structurally complex, typically composed of layers of saturated snow (snow-ice), frazil ice, and vertical columnar crystals. Microstructure and chemistry vary with depth due both to formation mechanism and a pronounced temperature gradient. Sea ice is  $-1.9^\circ\text{C}$  at the basal (ice-water) interface but considerably colder at the top (air-ice) interface (e.g.,  $-20^\circ\text{C}$ ) [Thomas and Dieckmann, 2009]. After the initial frazil layer coalesces, the ice grows downward as a result of heat flux to the (cooler) surface. This produces columnar crystals of nearly freshwater ice [Weeks and Ackley, 1982]. Brine channels form as salt is expelled from the freezing water and form networks that allow gas and fluid transport up and down in the ice cover over time. Even in very cold conditions where liquid is not apparent on the surface, sea salt is wicked up by frost flowers growing on the sea ice, by the snowpack, and by snow blowing across the sea ice, all of which have greater surface area than the sea ice surface and thus provide good locations for heterogeneous chemical reactions [Rankin *et al.*, 2002; Perovich and Richter-Menge, 1994; Eicken *et al.*, 1994; Massom *et al.*, 2001; Dominé *et al.*, 2004, 2005; Yang *et al.*, 2008; Obbard *et al.*, 2009]. We are interested in the roles that sea ice and blowing snow play in tropospheric chemistry in the sea ice region.

The samples examined for this study come from ice cores collected from land fast sea ice on the Ross Sea, Antarctica, in October 2012. We also collected snowpack and blowing snow samples, water salinity, and temperature data from these sites, but those data are reported elsewhere [Lieb-Lappen and Obbard, 2015]. Whole sea ice cores were transported back to our lab in Hanover, New Hampshire, where we ran a suite of microstructural and chemical analyses—optical microscopy, microcomputed X-ray tomography, and ion chromatography. Results from those analyses are described elsewhere [Lieb-Lappen and Obbard, 2015] or are in preparation.

In addition to the data derived from those techniques, we wanted to understand the distribution of halogen species, particularly bromine, with respect to the sea ice microstructure: ice crystals, grain boundaries, brine pockets, and bubbles. This information would help explain the potential for diffusion of bromine compounds through the sea ice cover.

To examine this requires a technique with high enough spectral resolution and spatial range to resolve individual salt constituents on grain boundaries (submicron scale) and in brine channels or pockets (millimeter-centimeter scale). Confocal Raman spectroscopy has been used to identify molecules and molecular ions in triple junction and water veins between sea ice crystals [Barletta *et al.*, 2009; Barletta and Dikes, 2015]. The Raman technique is not suitable for single ions, however, and would not reveal the presence of  $\text{Br}^-$  or  $\text{Cl}^-$ . Energy-dispersive spectroscopy (EDS) using a scanning electron microscope (SEM) has much higher spatial resolution (submicron, at least, for ice samples), and we have established a technique for the imaging and acquisition of EDS data from uncoated ice [Cullen and Baker, 2000]. There are several disadvantages inherent in SEM/EDS, however. One is that electron beams do not penetrate far into the sample, so only elements exposed on the surface are detected. Salts are concentrated primarily in exposed brine channels, but the process of microtoming the sample prior to SEM will tend to redistribute them across the surface. There are alternative surface preparation techniques, such as allowing controlled sublimation in the SEM to expose a fresh surface [Prior *et al.*, 2015]. This however may concentrate salts in locations where they lie. The advantage to X-ray analysis techniques is that the lower absorption cross section of X-rays allows deeper penetration into the sample and three-dimensional analysis without sectioning.

Several other researchers have used synchrotron techniques on natural sea ice, but few have used them to examine the location of specific salts. The first experiments segmenting pore structures in sea ice with synchrotron X-ray microtomography (SXRT) were done by Eicken and Miner in 2005 at the GeoSoilEnviroConsortium for Advanced Radiation Sources (GSECARS) beamline of the Advanced Photon Source (APS; Argonne National Laboratory, Illinois, USA) (unpublished, per private correspondence). The first published work demonstrating the use of SXRT is by Maus *et al.* [2009], who used the TOMCAT beamline of the Swiss Light Source (SLS; Paul Scherrer Institute, Villigen, Switzerland). They analyzed centrifuged samples at a temperature of  $-30^\circ\text{C}$  and produced images with a  $5.6\ \mu\text{m}$  voxel size. They also experimented with non-centrifuged samples of laboratory grown sea ice that had been cooled below  $-50^\circ\text{C}$  after sampling but found that the results suffered from the deep-freezing process.

During that same period, Hutterli *et al.* [2008] also used SXRT at SLS (MSTOMO and TOMCAT beamlines) to examine the location of bromine in laboratory-grown frost flowers produced on 2–15  $\mu\text{L}$  droplets of a

**Table 1.** Ice Texture as a Function of Depth in Sea Ice Cores from the Butter Point, Iceberg, and Scott Base Sites

Core	Granular (cm)	Columnar (cm)	Platelet (cm)
Butter Point (MC1)	0–14	14–65	65–180
Iceberg (MC4)	0–30	30–137	137–189
Scott Base (MC16)	0–91	91–144	144–202

NaCl-NaBr solution and cooled during SXRT with a cryojet. They used X-ray energies between 13.2 keV and 13.8 keV, i.e., below and above the K absorption edge of bromine. The 500 to 1500 projections with a nominal resolution of 0.7  $\mu\text{m}$  (often

binned to 1.4  $\mu\text{m}$  to reduce noise) were then reconstructed to reveal the brine channels and distribution of Br within the droplet.

In this paper, we describe our application of synchrotron X-ray fluorescence spectroscopy (SXRF) to examine the distribution of salts in sea ice.

## 2. Methods

### 2.1. Sample Collection and Preparation

The sea ice we examined came from the McMurdo Sound, Antarctica, in October–November 2012. One field site, called “Butter Point,” was located 35 km north of the McMurdo Ice Shelf and 5 km from the open ocean. Our other field site, “Iceberg Site,” was located 55 km northwest from the first but also approximately 5 km from open water. We also collected a multiyear sea ice core behind Cape Armitage, our “Scott Base” site. There were significant differences between the cores, most likely a function of their locations with respect to circulation in the Ross Sea and flow of Ice Shelf Water from the cavity beneath the Ross Ice Shelf [Robinson *et al.*, 2014].

Immediately after withdrawing the cores from the ice, we measured the internal temperature of each at 10 cm intervals along its length. Temperatures in the top centimeter (henceforth labeled “0 cm”) ranged from  $-7^{\circ}\text{C}$  to  $-18^{\circ}\text{C}$ . Temperatures near the bottom were approximately  $-2^{\circ}\text{C}$ . The cores and all samples were stored temporarily in a  $-20^{\circ}\text{C}$  freezer at nearby McMurdo Station and later transported to Dartmouth College. An accompanying low-temperature data logger showed that they remained below  $-20^{\circ}\text{C}$  during shipping. In Dartmouth’s Ice Research Laboratory, they were stored in a  $-33^{\circ}\text{C}$  freezer, except while cutting them in a  $-15^{\circ}\text{C}$  cold room. Brine that does not drain from the ice as the core is pulled from the borehole remains in brine pockets or channels. We saw little brine drainage from these cores during collection and none during processing.

Each core was cut in half along its long axis, and vertical thin sections (0.5 mm thick) were prepared for each entire core. The vertical thin sections (not shown) revealed, from top to bottom, granular ice, columnar ice, and platelet ice. The depths at which each structure is found at the different sites, shown in Table 1, are discussed briefly here and will be referenced later in section 4.

Granular sea ice, produced by the freezing of frazil ice, and possibly the incorporation of snow cover as snow ice, is relatively fine grained and equiaxed compared to congelation ice. The latter is distinguished by its long (1–10 cm) columnar crystals and lamellar texture, with brine layers spaced 0.4–1.0 mm apart [Harrison and Tiller, 1963; Paige, 1966; Jeffries *et al.*, 1993]. Although there was little snow cover at the Butter Point and Iceberg sites, the multiyear sea ice off Cape Armitage was covered by 1.5 m of snow, and the surface of the ice was below freeboard. Hence, some of the 91 cm of granular ice in the Scott Base core is likely snow ice. A good part of each core (28% at Butter Point, 57% at Iceberg, and 26% at Scott Base) was columnar ice, and below that was platelet ice. Platelet ice is formed in areas adjacent to subglacial melting, where buoyant plumes of fresh meltwater emerge from depth and rise to meet the base of floating ice. Thus, platelets of freshwater ice formed from the supercooled melt consolidate on the underside of growing sea ice [e.g., Weeks and Ackley, 1982; Lange, 1988; Tison *et al.*, 1993]. Platelets are thin (e.g., 1–5 mm) relative to their width (e.g., 20–30 cm) and easily distinguished in vertical thin sections from columnar ice by their more equiaxed dimensions and random orientations. Platelet ice made up the lowest portion of each core, but its significance as a percentage of the overall core varied (64% at Butter Point, 28% at Iceberg, and 28% at Scott Base), presumably as a function of proximity to the freshwater source (under shelf melting).

Horizontal thin sections were prepared for samples taken to Argonne National Laboratory. At 10 cm intervals, three small pieces, each approximately 10 mm  $\times$  20 mm  $\times$  5 mm, were cut perpendicular to the core axis, with

a band saw, and the edges smoothed with razor blades. Samples were transported to Argonne National Laboratory in a polystyrene foam cooler with dry ice and  $-20^{\circ}\text{C}$  blue ice packs. This storage and transport protocol, while typical for sea ice cores, is not ideal because it means that some ice, i.e., the deeper sections, is held at much colder temperatures than it experienced in situ. When sea ice is subjected to colder than in situ temperatures, some of the remaining liquid component freezes, and solid salts may precipitate [Light *et al.*, 2003]. If these samples are later warmed, some of the brine can become liquid again. There are also pressure changes associated with the temperature fluctuations. The fine submillimeter microstructure can be altered by this cycle [Maus *et al.*, 2009], and changes are irreversible [Lieb-Lappen and Obbard, 2012].

In horizontal thin sections, columnar ice appears as well-organized parallel crystals with parallel sets of brine layers interposed between the broader plates of ice. Platelet crystals may be distinguished by having a larger range of sizes, being more randomly organized and having less straight (or even wavy) crystal edges [Jeffries *et al.*, 1993; Dempsey *et al.*, 2010; Dempsey and Langhorne, 2012].

## 2.2. Synchrotron X-ray Fluorescence Spectroscopy

SXRF was performed on beamline 13-ID-E at APS in March 2013, March 2014, and August 2014. GeoSoilEnviroCARS (GSECARS) operates a hard X-ray microprobe at APS Sector 13 for synchrotron-based research on Earth materials. A 2.1 m undulator provides a tunable X-ray source (with an energy range from 2.4 to 28 keV and a spectral resolution of approximately 1 to 4 eV). The X-ray energy was selected with a Si (111) monochromator, and the monochromatic beam focused to a spot of approximately  $2\ \mu\text{m} \times 4\ \mu\text{m}$ . The sample was positioned with the help of a visible light CCD camera and motorized stages with submicron precision. A SII Vortex ME-4 four-element silicon drift diode array detector was used to detect X-ray fluorescence from the sample. We scanned  $2\ \text{mm} \times 2\ \text{mm}$  areas of the sample, scanning continuously and collecting the entire X-ray fluorescence spectrum at 0.1 s increments, integrating over  $10\ \mu\text{m}$  per pixel. This allowed us to map the location of the primary elements of interest (Cl and Br), as well as K, Ca, Sr, Fe, Zn, and Cu. Typical detection limits for ions in aqueous solutions with this instrumentation range from around 50 ppm for Cl and S to around 1 ppm for Br.

The samples were fixed by press fit or held with a few drops of water on the edges in small acrylic frames that slid into a slot in the cold stage. The cold stage, built by GSECARS, consists of a Peltier thermoelectric module cooled by a circulating ethylene glycol-water mixture. Kapton<sup>®</sup> brand polyimide film ( $8\ \mu\text{m}$  thick) was used to cover the sample (preventing the formation of frost on the surface). Sample temperatures during testing were between  $-15.9$  and  $-22.0^{\circ}\text{C}$ . The sample to detector path length was approximately 8 mm.

The penetration depth or distance at which the X-ray strength has been reduced to  $1/e$  (about 37%) of its original strength of 18 keV incident energy X-rays in water is 9.6 mm [Elam *et al.*, 2002]. Because the angle of the incident beam was  $45^{\circ}$  to the sample surface, the penetration would be reduced by 71%. Nonetheless, the beam penetrates the full 5 mm thickness of our samples, and only 0.3% of incident X-rays is absorbed. To reduce the possibility of sampling multiple grains in a single pixel, we had selected samples with grain boundaries that were nominally perpendicular to the sample surface.

The energy of the emitted photon is characteristic of the element from which it fluoresced. For Br, the K absorption edge is found at 13.474 keV and the fluoresced  $K_{\alpha}$  peak, corresponding to a drop from an L3 electron, occurs at 11.924 keV [Elam *et al.*, 2002]. Chlorine is of lower atomic number ( $Z=17$ ) than bromine ( $Z=35$ ), and thus, its characteristic X-rays are lower energy. The K absorption edge is 2.822 keV, and the fluoresced  $K_{\alpha}$  peak is found at 2.622 keV [Elam *et al.*, 2002]. The emitted photon then must travel out of the sample and a linear path of air before striking the detector. Since the emitted photon is at a lower-energy level than the incoming beam, the penetration depth is smaller for the fluorescence signal. For Br  $K_{\alpha}$ , this distance is 3.1 mm [Elam *et al.*, 2002]. (The angle of the detector is also  $45^{\circ}$  to the sample surface, so this would be attenuated as described for the incident beam.) Thus, although the incoming beam penetrates the entire sample thickness, detected Br signal is only from the top 3.1 mm. Due to the lower-energy emitted photons for Cl, the penetration depth for  $K_{\alpha}$  in water ice is only  $35\ \mu\text{m}$ . Thus, the chlorine detected in the samples is only from the topmost  $35\ \mu\text{m}$ , while the bromine is from 3.1 mm. Table 2 provides the critical energies and penetration depth for each of the elements analyzed.

X-ray attenuation can occur in the linear path of air between the sample and the detector. Enclosing the entire experimental setup in a helium-filled zippered polyethylene bag reduces this and helped to increase

**Table 2.** SXRF Energies and Penetration Depth for Elements Discussed in This Paper<sup>a</sup>

Element	K Absorption Edge (keV)	K <sub>α</sub> Peak Location (keV)	Detector Energy Range (keV)	Fluorescence Penetration Depth (mm)
Br	13.474	11.924	11.63–12.27	3.1
Cl	2.822	2.622	2.47–2.72	0.035
K	3.608	3.314	3.11–3.42	0.069
Ca	4.039	3.692	3.49–3.87	0.095
Sr	16.105	14.165	13.67–14.57	5.1
Fe	7.112	6.405	6.12–6.66	0.49
Zn	9.659	8.637	8.36–8.93	1.2
Cu	8.979	8.046	7.75–8.31	0.98

<sup>a</sup>These have not been adjusted for incident and detection angles.

the photon count at the detector for all elements. This was particularly important for low-energy Cl, K, and Ca detection. Under these conditions, we were able to obtain X-ray spectra such as those shown in Figure 1.

During the 2014 visit, we also analyzed a blank Milli-Q water sample and two liquid standards to find a calibration curve enabling the estimation of concentration from elemental XRF maps. Although replicating the sample setup (n) with frozen samples would be ideal, it was not possible to create such a standard as the freezing process rejects impurities leaving a nonhomogeneous product. The measured photon count of the region scanned would then not be representative of the desired standard concentration. However, the difference in X-ray penetration depth between water and ice is negligible for the X-ray energies encountered in this study [Elam et al., 2002]. Other than the phase difference, the rest of the experimental setup was kept constant, including the thickness of the sample. The two standards contained 0.5 g/m<sup>3</sup> (μg/cm<sup>3</sup>) (Standard A) and 2.0 g/m<sup>3</sup> Br (Standard B) and 25 g/m<sup>3</sup> (Standard A) and 100 g/m<sup>3</sup> Cl (Standard B) and were analyzed over 120 s. The peaks in the standards corresponding to Cl fluorescence were too close to the baseline signal for accurate standard calibration. Thus, concentration estimation was only possible for Br elemental maps.

The major peaks are labeled in Figure 1. Noticeable in all spectra is the sharp dropoff in photon count at 18 keV, the energy level of the incoming X-ray beam, and the smooth decay in photon count just below 18 keV due to Compton scattering. Measurable in most sample spectra were peaks corresponding to Cl K<sub>α</sub>, K K<sub>α</sub>, Ca K<sub>α</sub>, Ca K<sub>β</sub>, Fe K<sub>α</sub>, Fe K<sub>β</sub>, Cu K<sub>α</sub>, Zn K<sub>α</sub>, Zn K<sub>β</sub>, Br K<sub>α</sub>, Br K<sub>β</sub>, and Sr K<sub>α</sub>. By integrating the area under each peak after a baseline correction, we arrived at an estimate of relative intensity of each element in each sample. Since the sample apparatus was not enclosed in a helium environment during the 2013 visit to APS, these

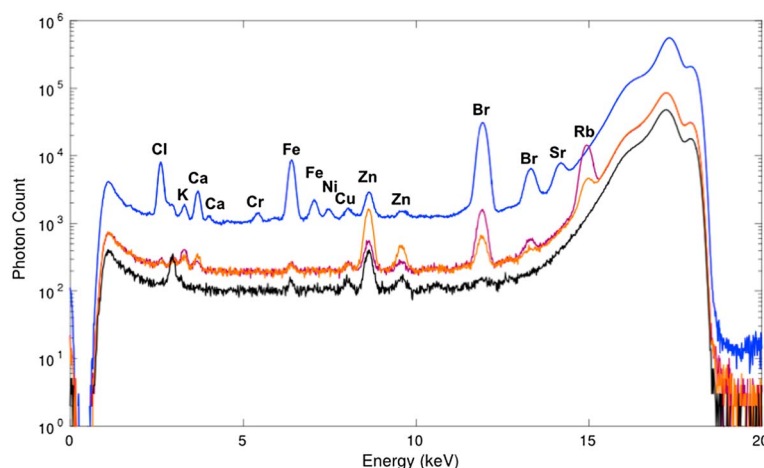


**Figure 1.** SXRF spectra for a typical sample (blue), standard A (0.5 g/m<sup>3</sup> Br and 25 g/m<sup>3</sup> Cl; orange), standard B (2.0 g/m<sup>3</sup> Br and 100 g/m<sup>3</sup> Cl; purple), and Milli-Q water (black). Incoming X-ray energy was 18 keV. Spectra represent the sum of the photon counts over all four detectors. Note however that the collection time differed between the sample spectrum and the standard spectra, and thus, there is an offset between the different baselines. Peaks common in many of the samples are labeled.

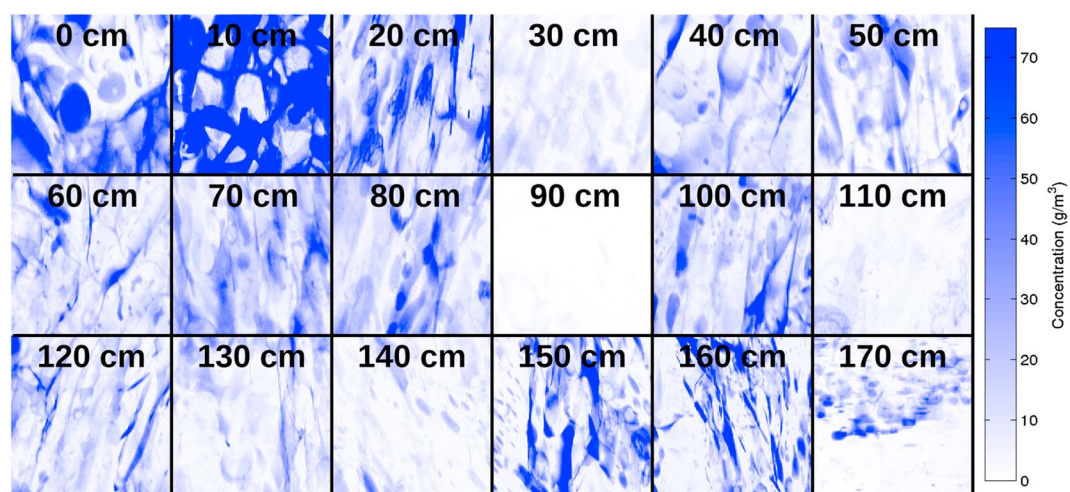


**Figure 2.** The 2 mm  $\times$  2 mm Br maps of the Butter Point ice core for subsamples taken at 10 cm intervals. The scale bar for the blue color indicates the intensity of the Br signal from low (white) to high (dark blue) and is calibrated to concentration using two standards as described later in the text.

samples did not exhibit peaks for the lighter elements such as Cl, K, and Ca. During that visit, fluorescent X-rays from the lighter elements were mostly absorbed by air in the path from the sample to the detector. Note that although samples contain much higher concentrations of Cl than Br, the spectra peaks are much stronger for heavier elements such as Br, since their fluoresced electrons can escape from a far greater depth.

### 2.3. Elemental Maps

To make an elemental map for each sample, the photon counts are summed over the desired energy levels for each pixel. For bromine, this corresponded to energy limits of 11.63–12.27 keV. We make a deadtime correction of the signal for each detector and then sum the photon counts over all four detectors. Raw photon counts were all scaled by the incoming beam flux to account for fluctuations in the source beam strength. For visual display of relative intensities, all values were then scaled to 0–255.

### 2.4. Comparison to Thin Sections

The Ultralene<sup>®</sup> window in front of the sample prevented precise visual location of the 2 mm  $\times$  2 mm regions scanned. Thus, for most of the analysis we have had to rely on feature size to compare our SXRF observations to microstructure. To better identify the features detected on elemental maps, horizontal thin sections of each sample were prepared after SXRF analysis. We attached the SXRF samples to glass plates, thinned them to approximately 0.5 mm, and photographed them between crossed polarizing lenses.

## 3. Results

Bromine maps for Butter Point (first-year ice), Iceberg Site (first-year ice), and Scott Base (multiyear ice) are presented in Figures 2–4, respectively. Clearly, bromine is not evenly distributed throughout the individual sample cross sections. There is also significant variability between depths in a single core and for the same depth in different locations.

Beginning at the snow-ice interface, the Br maps for the topmost sample for both first-year ice cores (Figures 2 and 3) show rounded features approximately 400  $\mu$ m in diameter. These rounded features are also somewhat visible in the samples from 10 cm and 20 cm for both cores. They are not as noticeable in the multiyear ice core collected near Scott Base (Figure 4). All three cores also exhibit very small circular features in the deepest samples, but this feature is more prevalent in the first-year ice cores.

The dominant feature throughout the bulk of all three of the ice cores is set of parallel lines, the spacing of which is on the order of magnitude of 0.5 mm. Exceptions to this include the sample from 40 cm in the Iceberg Site core and samples from 30 cm and 120 cm in the Scott Base core.

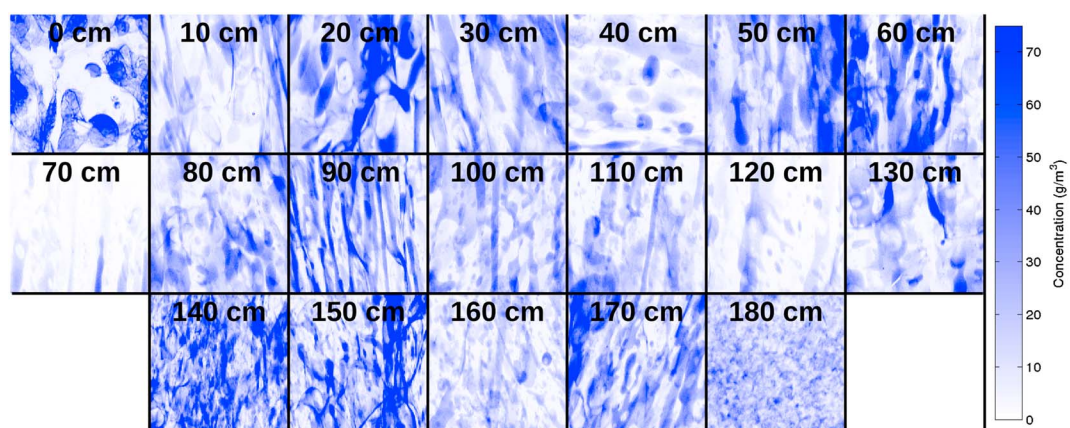


**Figure 3.** The 2 mm × 2 mm Br maps of the Iceberg Site ice core for subsamples taken at 10 cm intervals. The scale bar for the blue color indicates the intensity of the Br signal from low (white) to high (dark blue) and is calibrated to concentration using two standards as described later in the text.

The Br elemental maps for the Scott Base core in Figure 4 did not have the same rounded features in the upper part of the core as did the first-year ice cores. However, there was indeed a transition occurring around 80–100 cm, but due to low concentrations of Br in these samples, it was difficult to pinpoint the precise depth of the transition point.

### 3.1. Br Concentration

We were able to convert the relative intensity of the Br signal for the elemental maps in Figures 2–4 since photon counts are directly correlated with concentration. To calibrate the signal, we analyzed two liquid standards and one blank Milli-Q water sample as in Figure 1. On all spectra, the baseline signal was first subtracted mathematically by estimating its signal within multiple shifted windows and then regressing the varying baseline to the window points using a spline approximation. Then, as described above for the sample maps, the photon counts were integrated over the Br  $K_{\alpha}$  energy range 11.63–12.27 keV. The deadtime corrected signal was then summed over all four detectors. Since standard spectra were collected over a longer time period, this count was scaled by 120/0.1 for comparison with sample spectra. Finally, the resulting numbers were scaled by the average incoming beam flux and normalized to the same scale as the sample elemental maps. Since the standard concentrations were known, this enabled us to convert the sample elemental maps from a 0 to 255 scale to a scale of concentration, as is shown in the scale bars for Figures 2–4. For the sample elemental maps, maximum Br concentrations were roughly 70 g/m<sup>3</sup> and generally occurred in the linear features described above.

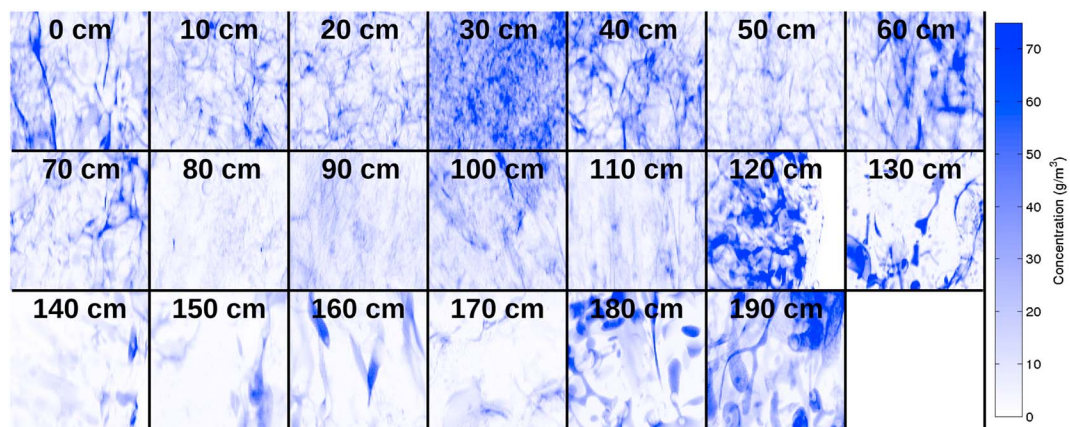


**Figure 4.** The 2 mm × 2 mm Br maps of the Scott Base ice core for subsamples taken at 10 cm intervals. The scale bar for the blue color indicates the intensity of the Br signal from low (white) to high (dark blue) and is calibrated to concentration using two standards as described later in the text.

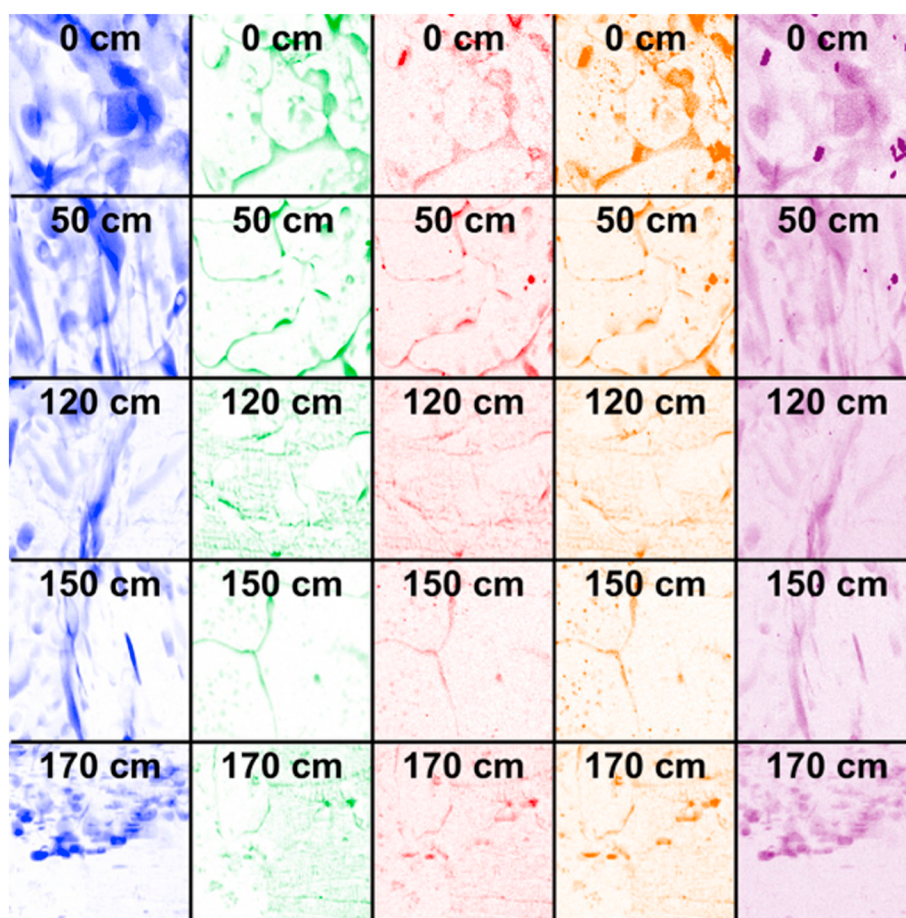


**Figure 5.** SXRF elemental maps for Br (blue), Cl (green), K (red), Ca (yellow), and Sr (purple) for subsamples taken at 10 cm intervals along the Butter Point ice core. For a given depth, all five images are from the same scan over a 2 mm  $\times$  2 mm region. For maps other than Br, we were unable to calibrate the signal into concentration. Thus, each map is colored in relative intensity from low (white) to high (darker shade of specified color).

### 3.2. Multiple Element Maps

By enclosing the experimental setup in a helium environment, we were able to map the locations of Cl, K, Ca, and Sr, as well as Br, during the 2014 visit to APS. Cl, K, Ca, and Sr peaks on the SXRF spectra were integrated between the energy limits shown in Table 1. This yielded elemental maps for each element similar to those shown above for Br. For this analysis, only a selection of subsamples from the Butter Point and Iceberg Site cores was used. Representative samples from each depth are shown in Figures 5 (Butter Point) and 6 (Iceberg Site). Note the similarity of the Br and Sr maps and of the Cl, K, and Ca maps.

Three subsamples were cut and analyzed from each depth. To examine how representative a mapped location was of a given sample, we mapped three different locations on each sample in 2014. Triplicate elemental maps for top, middle, and bottom depths of the Butter Point and Iceberg Site cores are shown in Figure 7. To assess reproducibility, we mapped the same area on one sample twice (not shown). Those maps appeared identical. Brine enclosures can range in diameter from submillimeter to centimeter, and to maintain sample integrity we were obliged to select samples containing only small ones. Further, these elemental maps are highly dependent upon the precise region analyzed, so we were concerned that a single map from one depth would not represent the majority of sea ice at that depth. Nonetheless, the maps do look similar.

Qualitatively, although there is variability among the replicates, many of the same features can be seen across samples of a given depth. For example, the topmost samples, from the Butter Point ice core in particular, show complex and fine-scale heterogeneity for all salts. The ice at this depth is entirely granular. At

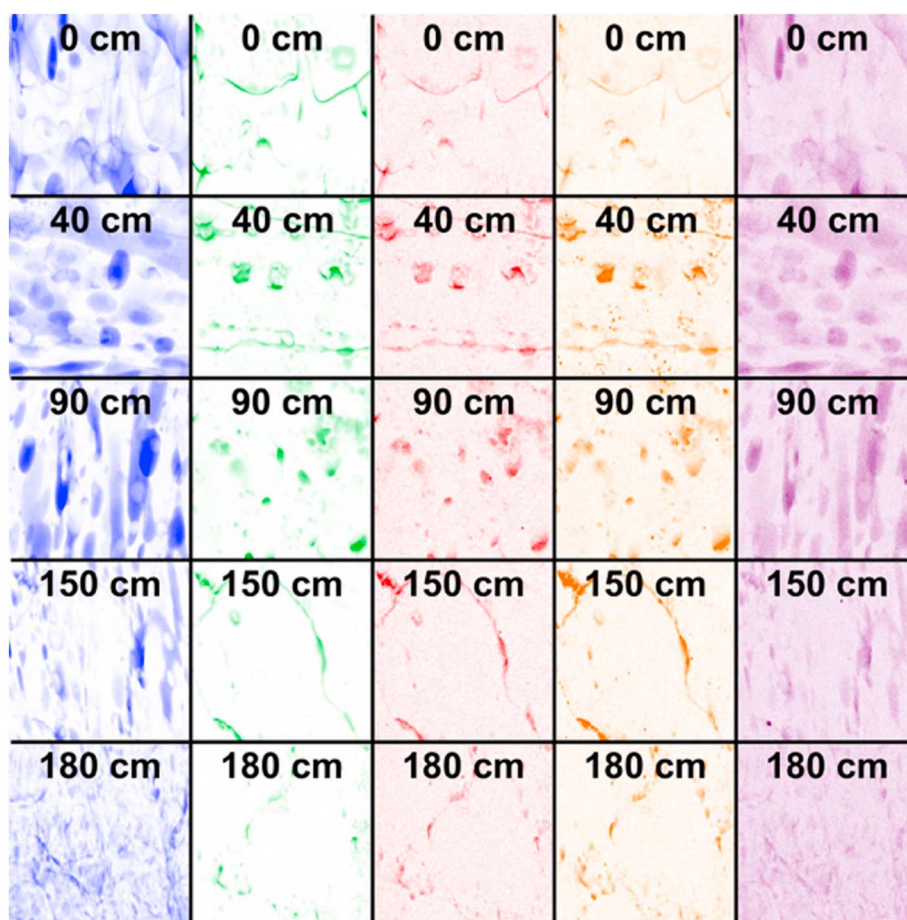


**Figure 6.** SXRF elemental maps for Br (blue), Cl (green), K (red), Ca (yellow), and Sr (purple) for subsamples taken at 10 cm intervals along the Iceberg Site ice core. For a given depth, all five images are from the same scan over a 2 mm × 2 mm area. For maps other than Br, we were unable to calibrate the signal into concentration. Thus, each map is colored in relative intensity from low (white) to high (darker shade of specified color).

middepths, the salts are primarily located at grain boundaries and in brine layers and channels across all replicates. The deepest samples for each core do not show a prevalence of grain boundaries. Although the salt concentration is relatively large at this depth, the salts are located throughout the scanned region. This could be evidence of some salt redistribution that occurs with the more significant temperature changes in ice which is in situ greater than  $-10^{\circ}\text{C}$ .

Despite the variability, there is a consistency to the shapes and sizes of features that appear in maps from a given core and depth. This allows us to begin analyzing the microstructural location of salts in sea ice.

### 3.3. Comparison to Thin Sections of Samples

Thin sections made of the SXRF samples provided a way to compare the elemental maps to microstructure, both generally, in terms of grain size and grain boundary and brine pocket spacing and more specifically as a way to interpret what we are seeing in individual maps.

Figure 8 presents the best direct matching found of SXRF images to horizontal thin sections. Two regions were located on a thin section from the 150 cm depth sample of the Iceberg Site core that are likely the regions scanned. As can be seen on the different elemental overlays, the grain boundaries visible in the thin section are well detected by the Cl, K, and Ca maps.

The lower region identified in Figure 8 was further examined to investigate particular features within the image. Two unique features of the Cl elemental map were isolated and are shown in Figure 9. The first was a small circular shape located in the middle of the image, while the second encompassed a portion of the

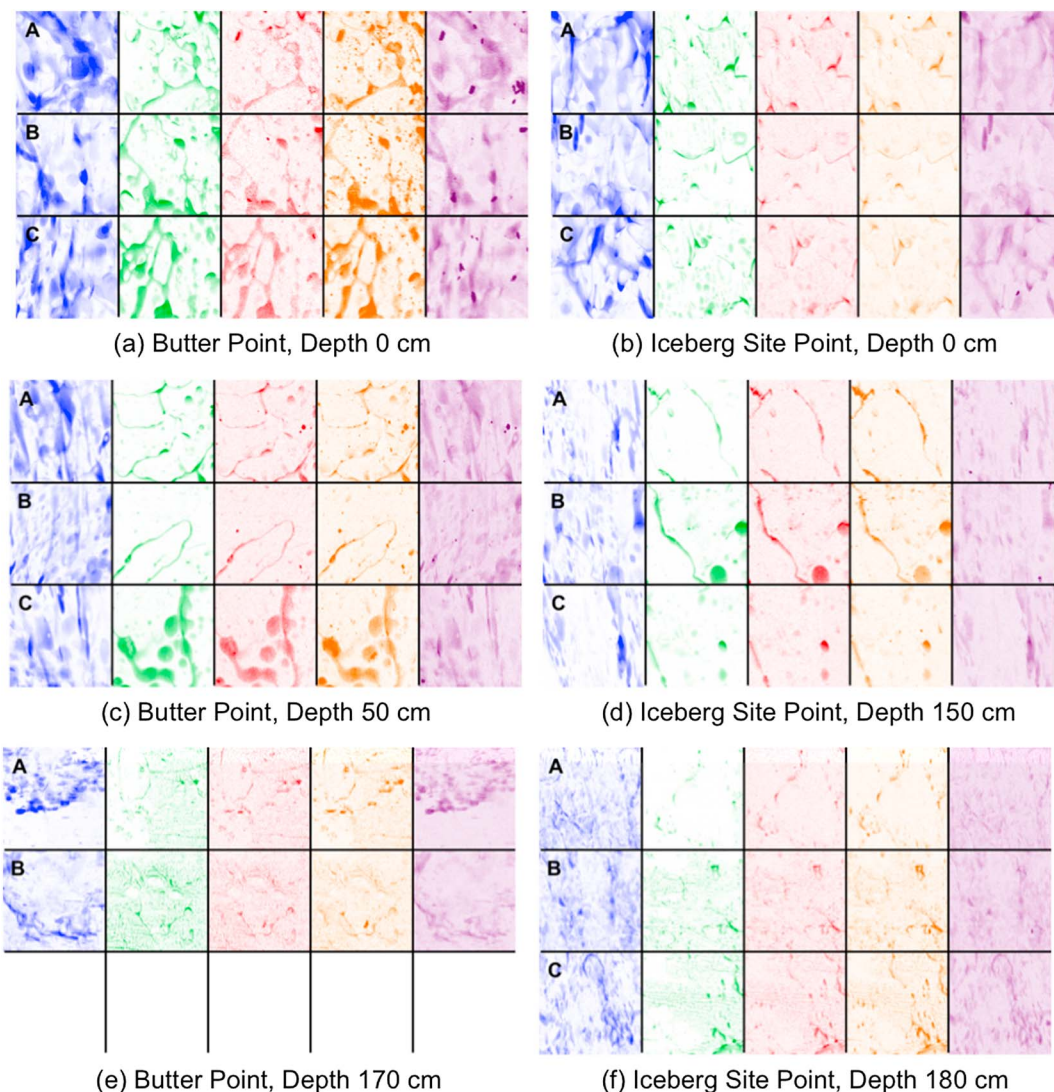
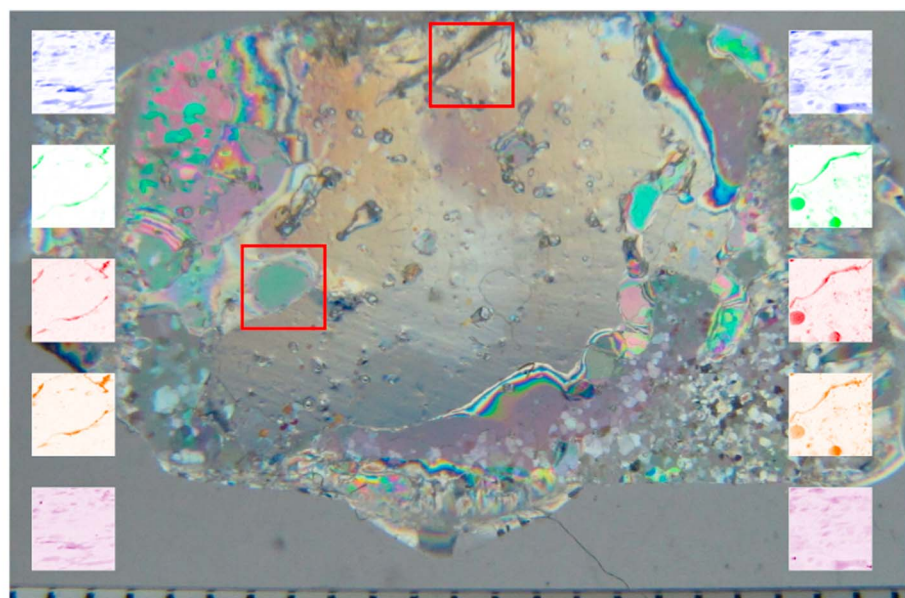


**Figure 7.** SXRF replicate elemental maps for Br (blue), Cl (green), K (red), Ca (yellow), and Sr (purple) for selected subsamples of the Butter Point and Iceberg Site ice cores. For a given depth and a given row, all five images are from the same scan over a 2 mm × 2 mm region. Each row represents a different sample for the given depth. For maps other than Br, we were unable to calibrate the signal into concentration. Thus, each map is colored in relative intensity from low (white) to high (darker shade of specified color).

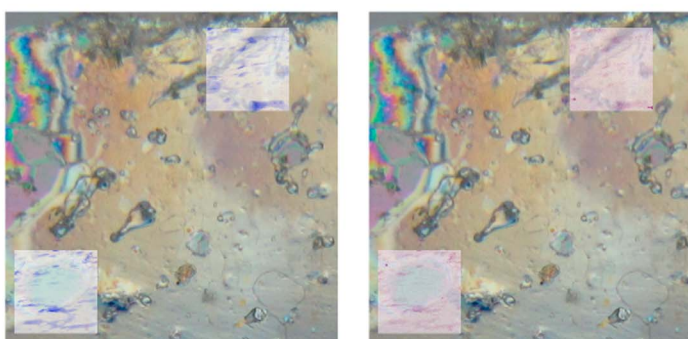
grain boundary. The SXRF spectra for these isolated features are compared to the spectra for the whole region in Figure 10. Both features had strong peaks corresponding to Cl (2.622 keV), as would be expected. The small circular feature however had large peaks corresponding to elevated Cr (5.415 keV), Fe (6.405 keV for  $K_{\alpha}$  and 7.059 keV for  $K_{\beta}$ ), and Ni (7.480 keV). These peaks are not present in the grain boundary spectrum nor was this feature visible in the thin section image (Figure 8). This suggests that it may be a dust particle or possibly even a fragment of the razor blade used to smooth the sample that was removed during preparation of the thin section. Although both feature spectra had peaks for K, Ca, Br, and Sr, the relative magnitude of the grain boundary spectrum peaks was greater.

#### 4. Discussion

Based on what is known about sea ice, we originally hypothesized that maps would show salts primarily in grain boundaries and brine pockets [Petrich and Eicken, 2009]. This has not been illustrated with microchemical maps before.

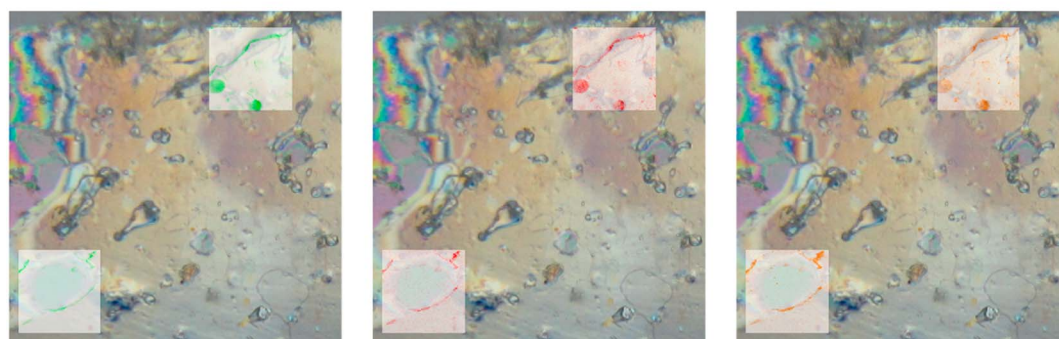


(a) Scanned Regions



(b) Br

(c) Sr



(d) Cl

(e) K

(f) Ca

**Figure 8.** Comparison of SXRf elemental maps to a horizontal thin section (tick marks are spaced at 1 mm intervals). (a) Two regions that were likely scanned from the 150 cm sample of the Iceberg Site core were located and are outlined with red boxes. (b–f) The blowups containing these regions with the Br, Cl, K, Ca, and Sr SXRf maps overlaid on top. The grain boundaries detected in the Cl, K, and Ca maps seem to match well with the grain boundaries visible from the horizontal thin section. Br and Sr maps appear to be detecting features from deeper within the sample. For maps other than Br, we were unable to calibrate the signal into concentration. Thus, each map is colored in relative intensity from low (white) to high (darker shade of specified color).

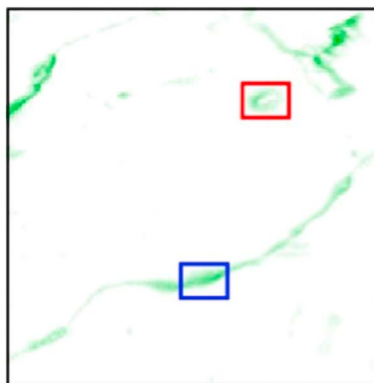


**Figure 9.** Two features of interest from the 2 mm × 2 mm Cl SXRF map. The sample is from a depth of 150 cm in the Iceberg Site ice core. The small circular shape in the middle is highlighted in red, while the second encompassing a portion of the grain boundary is shown in blue. For Cl, we were unable to calibrate the signal into concentration. Thus, the map is colored in relative intensity from low (white) to high (bright green).

The largest concentrations of Br, roughly 70 g/m<sup>3</sup>, were found in the linear brine layers. This is consistent with previous observations of 10–100 times greater brine salinity than bulk salinity [e.g., *Notz et al.*, 2005; *Weeks and Ackley*, 1982]. Although not a perfect proxy, considering both the three-dimensional character of the measurement and the great spatial variability, it is encouraging to note that the averaged value over all samples and all pixels is roughly 5 g/m<sup>3</sup>. This value is relatively close to the bulk concentrations measured in samples using ion chromatography.

We further hypothesized that elemental maps for Br and Cl would contain the same geometrical features as thin sections, i.e., grain boundaries and brine features. This proved to be true, as Cl, K, and Ca maps clearly show features that correspond to those visible in the thin section (Figure 8). Both SXRF and thin section images show small circular features of the same size that are likely brine channels. It should be noted here that the 45° angle of beam and detector to the sample, which had nominally vertical brine channels, will have blurred some features and stretched some by a factor of 1.414, but this correction does not change our overall results. Rounded features are visible in the uppermost Br maps for the first-year ice cores (Figures 2 and 3) but not as noticeable in the multiyear ice core collected near Scott Base (Figure 4). This may be because the Scott Base core, under 1.5 m of snow, had at some point had some freshwater (snow) melt which was incorporated when freezing resumed. In the deepest samples, small circular features are most noticeable in the first-year ice cores. The platelet sea ice at the base of our first year sea ice cores is “bladed” platelet texture, whereas the ice at the base of the Scott Base core is a “draped” platelet morphology [*Jeffries et al.*, 1993]. This

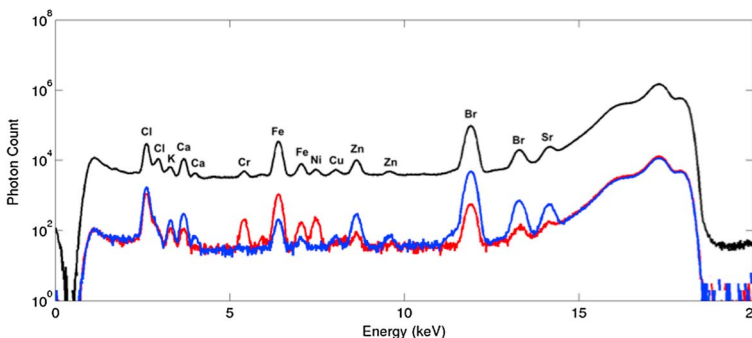


**Figure 10.** SXRF X-ray spectra for the 150 cm sample of the Iceberg Site core (black) and two features of interest. The circular shape identified in Figure 9 is shown in red, and the grain boundary selection is shown in blue. Note that because the blue and red regions are integrating over a smaller region than the full 2 mm × 2 mm region shown, they have a lower baseline than the full spectrum shown in black. The XRF spectra from both visits to APS contained peaks at 6.405 keV, 8.046 keV, and 8.637 keV, corresponding to Fe, Cu, and Zn, respectively. Trace metals found in Antarctic sea ice come from dust, upwelling, resuspension of shelf sediments, and remineralization. These are of interest to the biogeochemical community [e.g., *Lannuzel et al.*, 2011].

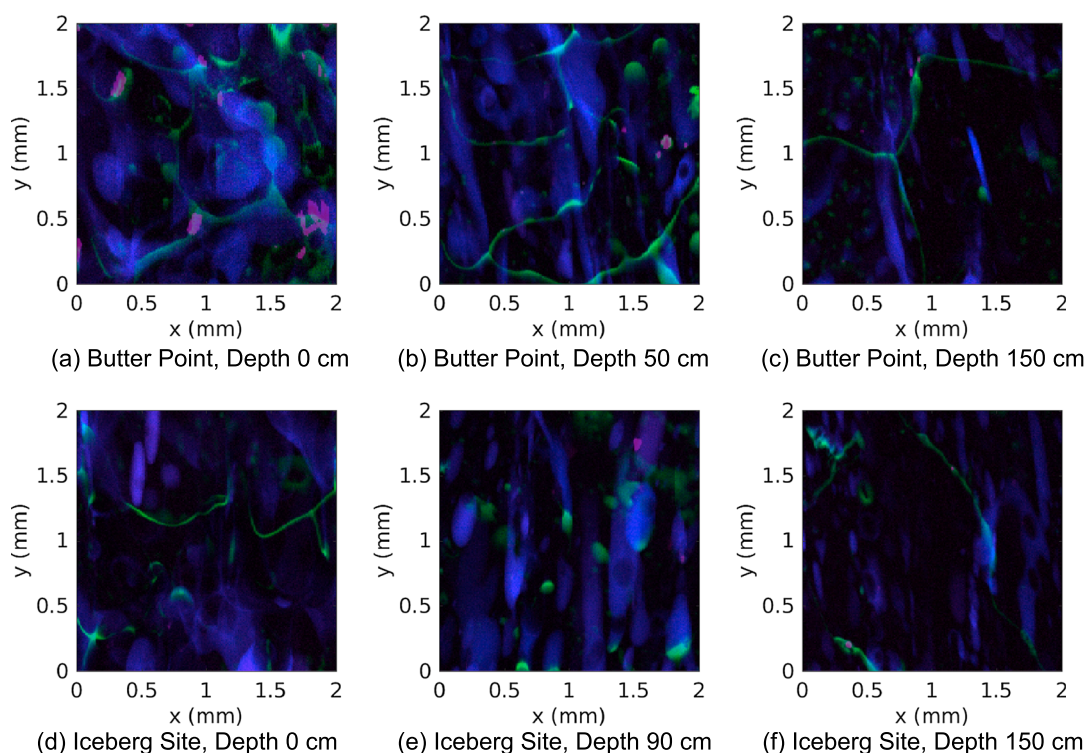


**Figure 11.** XRF elemental overlay maps showing Br, Cl, and Sr for selected subsamples. (a) Butter Point, depth 0 cm; (b) Butter Point, depth 50 cm; (c) Butter Point, depth 150 cm; (d) Iceberg Site, depth 0 cm; (e) Iceberg Site, depth 90 cm; and (f) Iceberg Site, depth 150 cm. For these images, blue represents Br, green represents Cl, and purple represents Sr. As before, each image shows the 2 mm  $\times$  2 mm region scanned. Note that for visual clarity, the relative intensity for each element is shown with black representing the absence of the particular element rather than white as in previous figures.

may explain the difference in feature shapes in elemental maps from these layers, but this hypothesis would need to be tested more thoroughly.

The transition from rounded features to sets of parallel lines having a spacing of 0.5 mm is consistent with the granular-columnar ice transitions, which are found at around 14 cm and 30 cm for the Butter Point and Iceberg Site core, respectively. Exceptions to this include the sample from 40 cm in the Iceberg Site core (which is near the granular-columnar interface). Elemental maps from 30 cm and 120 cm in the Scott Base core also represent exceptions. The entire top 80 cm of the Scott Base core was granular. We recorded the columnar-platelet transition in this core at around 144 cm (Table 1), but the transition from columnar to platelet ice is not sharp and can extend over a depth of 20–30 mm [Dempsey *et al.*, 2010]. So it is entirely possible that there was a mixture of platelets and columnar crystals at 120 cm.

The Br and Sr maps show additional features that are not visible in the thin sections. Due to their greater penetration depth, these elemental maps are likely detecting features from deeper within the sample, such as brine inclusions or dust not visible in the thin section that was imaged.

#### 4.1. Correlation Between Different Salts

To better visualize the different correlations among elements, three-element overlay maps were created for select few samples. Overlay Br, Cl, and Sr maps for samples from Butter Point and Iceberg Site cores are shown in Figure 11. The blue and purple from Br and Sr maps generally coincide. There are regions, however, that appear brighter blue or lighter purple, indicative of primarily Br or Sr, respectively, for example, at a depth of 0 cm for Butter Point where there are several purple circles about 100  $\mu$ m in size. The green in these figures suggest that Cl maps are detecting different features than Br/Sr maps. As mentioned earlier, this very well may be due to differences in penetration depth for Br/Sr versus Cl. In general, the green regions are restricted to lines measuring tens of microns in width, suggesting that Cl is mapping grain boundaries. We note the appearance of some green 100  $\mu$ m circles, such as in the maps from 50 cm for Butter Point and

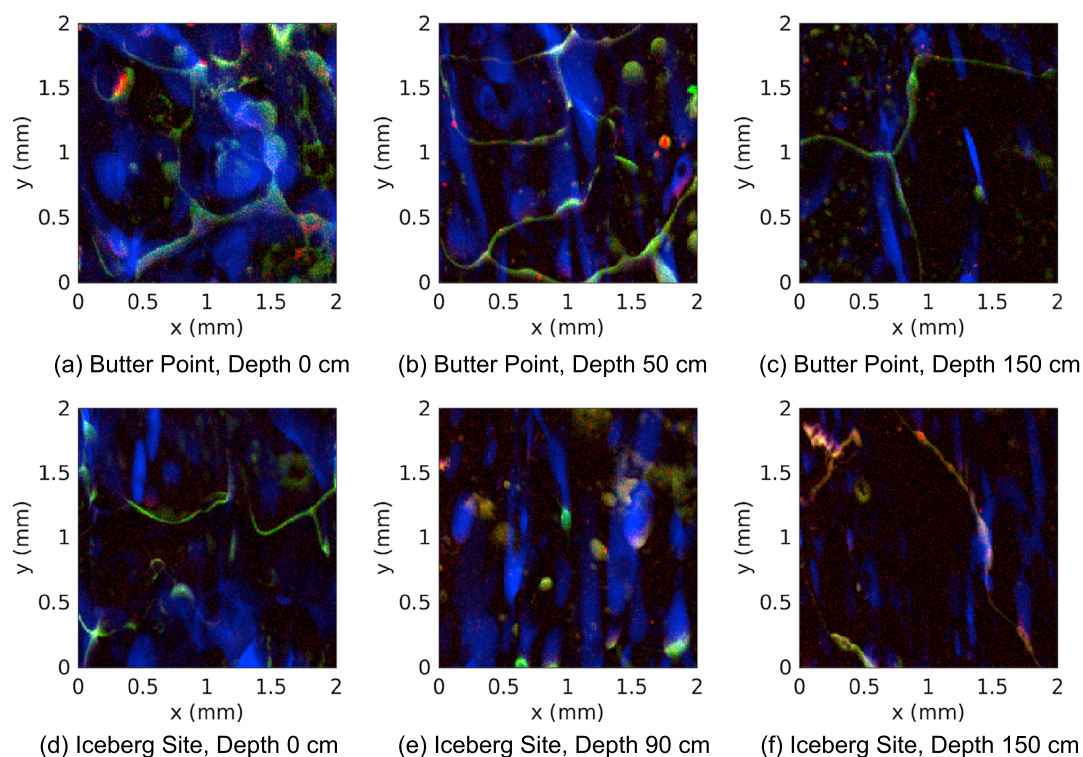


**Figure 12.** XRF elemental overlay maps showing Br, Cl, and K for selected subsamples. (a) Butter Point, depth 0 cm; (b) Butter Point, depth 50 cm; (c) Butter Point, depth 150 cm; (d) Iceberg Site, depth 0 cm; (e) Iceberg Site, depth 90 cm; and (f) Iceberg Site, depth 150 cm. For these images, blue represents Br, green represents Cl, and red represents K. As before, each image shows the 2 mm × 2 mm region scanned. Note that for visual clarity, the relative intensity for each element is shown with black representing the absence of the particular element rather than white as in previous figures.

90 cm for Iceberg site. In Figure 12, we replace Sr with K to yield slightly different three-element overlap maps. Here it becomes apparent that some of the features detected with Sr, but not Br, also contain K. In addition, the green Cl regions take on a lighter/increased yellow shade, indicating the co-location of Cl and K. We note that Ca maps have a similar trend and effect as K maps.

To quantify the co-location of the elemental maps, we calculated the Pearson’s linear correlation coefficients for each pair of elements for each sample. The matrix of average correlation coefficients is presented in Table 3. The correlation coefficient of 0.81 between Br and Sr indicates a clear co-location between the two elements.

Further, the high pair-wise correlations between Cl, K, and Ca suggest that they are mapping similar features. The individual correlation matrices for each sample of Butter Point and Iceberg Site cores are depicted in Figure 13, with the colors blue, green, red, black, and magenta signifying Br, Cl, K, Ca, and Sr, respectively. The mean over all samples for each element is shown as a thick dotted line and matches the data in Table 3. Each line peaks at 1 for its respective element as each is correlated with itself by definition.

**Table 3.** Matrix of Mean Correlation Values for Relative Amounts of Br, Cl, K, Ca, and Sr<sup>a</sup>

	Br	Cl	K	Ca	Sr
Br	1				
Cl	0.23	1			
K	0.25	0.73	1		
Ca	0.30	0.74	0.65	1	
Sr	0.81	0.20	0.24	0.29	1

<sup>a</sup>For each SXRF map, the correlation between each pair-wise set of elements was calculated. The mean value over all samples is given below.

Although there are some variabilities among the samples, the mean values represent the overall trends.

To gain further insight into the microstructural location of the different salts, principal component analysis was run on the collection of elemental maps for each sample. The five resulting components and the relative input from each element are shown in Figure 14, where the lines

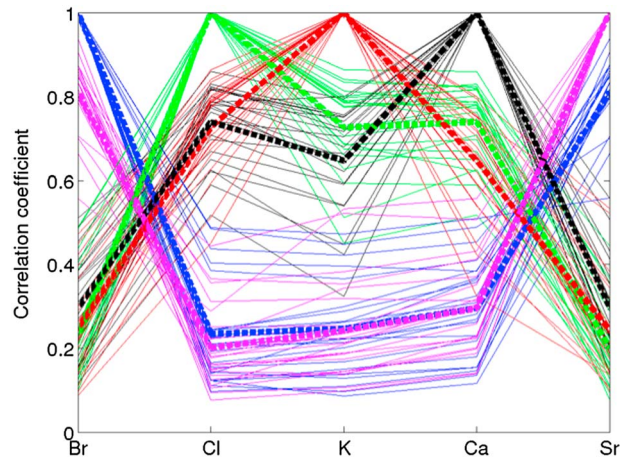


**Figure 13.** Pair-wise correlation values of different elements for all samples, with each color corresponding to a particular element. The colors blue, green, red, black, and magenta signify Br, Cl, K, Ca, and Sr, respectively, and each line represents a different SXRF map. The thicker dashed lines represent the mean values across all SXRF maps. Each element is by definition correlated to itself and thus has a value of 1. High values for other elements signify correlation between the two elements (e.g., Br and Sr).

for a particular component are different samples. The final plot of Figure 14 displays the normalized eigenvalues of the covariance matrix, which yield an indication of the relative importance each component plays to the total variance in the image. For this plot, the red lines are for Butter Point and the blue lines are for Iceberg site cores. As can be seen in the figure, the first principal component tends to account for 50–75% of the total

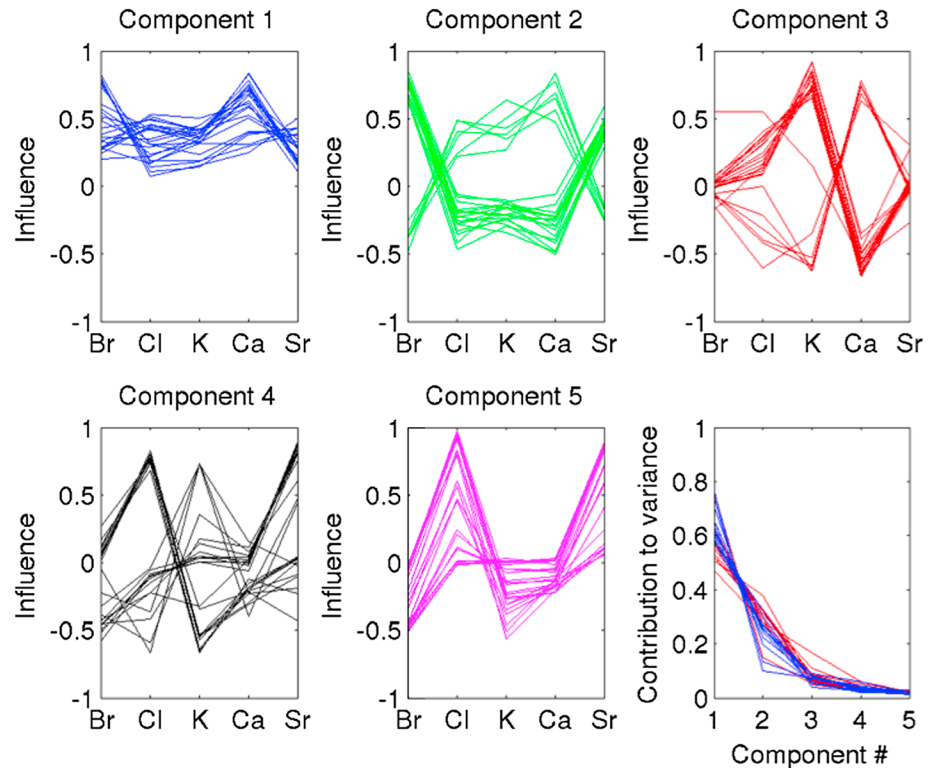


**Figure 14.** Principal component analysis of all subsample SXRF maps. The first five plots show the relative contribution of each element to the respective principal components, where each color is representing a different component and each line represents a different subsample. The final plot shows the normalized eigenvalues of the covariance matrix, which yield an indication of the relative importance each component plays to the total variance in the image. Here the blue and red lines represent the Butter Point and Iceberg Site ice core samples, respectively.

variance. Meanwhile the second component accounts for 15–30%, while the final three components have very minor effects. The first component has influences from all five elements, with not large fluctuations among the different salts. This is likely picking up the signal that all elements are found in brine regions but not throughout the bulk ice. The second component appears to split the samples into two groups, likely based on penetration depth. Many of the samples show a large influence from the Br/Sr signal, while a few show stronger influences from the Cl, K, and Ca signal. This second component suggests that generally, most of the variance within an image is due to the Br/Sr signal. The third, fourth, and fifth components appear to pick out differences among K, Cl, and Ca, with Sr occasionally being related.

## 5. Conclusions

SXRF is an excellent technique to examine the distribution of salts within the microstructure of sea ice. We have successfully utilized the technique to map the microstructural location of various impurities in sea ice and quantified the distribution of Br, an element of importance to the understanding of boundary layer atmospheric chemistry. By enclosing the experimental setup in a helium environment, it was possible to also map the location of lighter elements. SXRF elemental maps showed co-location of Br and Sr, as well as co-location of Cl, K, and Ca. This is most likely due to differences in the penetration depth for each element, where the Br and Sr fluorescence signal is from the top 3–5 mm, while the signal from Cl, K, and Ca is only from the top 100  $\mu\text{m}$ . This enables the simultaneous identification of different features in the sea ice microstructure.

We have also noted the tendency of different elements to highlight specific features of the sea ice. Through comparison with horizontal thin sections, we could verify that surface linear features in the Cl, K, and Ca maps represented grain boundaries. Br and Sr elemental maps identified deeper features. Throughout the bulk of our sea ice cores, salts tended to be concentrated in sets of parallel lines spaced roughly 0.5 mm apart, which corresponds to the spacing of lamellae in the skeletal region during columnar growth [Harrison and Tiller, 1963]. Variations from this structure were found primarily near the top of each core where granular ice is present and at the very bottom of each core where platelet ice is present. Calibration of the Br elemental maps showed bulk concentrations to be 5–10  $\text{g}/\text{m}^3$ , with concentrations ten times larger in the brine layers. This suggests that in most of the core, salts remain in brine inclusions. Also, importantly for those studying the transport of bromide ions to the tropospheric boundary layer, these results demonstrate the presence of Br in brine structures throughout the sea ice.

Finally, by examining the fluorescence signal for particular trace metals, it is also possible to isolate particular features that are likely dust and sediment particles trapped in the sea ice.

## Acknowledgments

This research was supported by US National Science Foundation (NSF) grant OPP-1043145 and the US Antarctic Program. The views and conclusions contained herein are those of the authors and should not be interpreted as representing official policies, either expressed or implied, of the NSF or the United States Government. We also acknowledge the support of Mark Rivers and GSECARS (APS Sector 13). GSECARS is supported by the National Science Foundation–Earth Sciences (EAR-1128799) and the Department of Energy, Geosciences (DE-FG02-94ER14466). The data associated with this research are archived in the NASA Global Change Master Directory and can be freely accessed at the following URL: <http://gcmd.nasa.gov/getdif.htm?NSF-ANT10-43145>.

## References

- Barletta, R. E., and H. M. Dikes (2015), Chemical analysis of sea ice vein  $\mu$ -environments using Raman spectroscopy, *Polar Rec.*, *51*(257), 165–176.
- Barletta, R. E., B. N. Gros, and M. P. Herring (2009), Analysis of marine biogenic sulfur compounds using Raman spectroscopy: Dimethyl sulfide and methane sulfonic acid, *J. Raman Spectrosc.*, *40*, 972–981.
- Barrie, L. A., J. W. Bottenheim, R. C. Schnell, P. J. Crutzen, and R. A. Rasmussen (1988), Ozone destruction and photochemical reaction at polar sunrise in the lower Arctic atmosphere, *Nature*, *334*, 138–141.
- Cullen, D., and I. Baker (2000), The chemistry of grain boundaries in Greenland Ice, *J. Glaciol.*, *46*, 703–706.
- Dempsey, D. E., and P. J. Langhorne (2012), Geometric properties of platelet ice crystals, *Cold Reg. Sci. Technol.*, *78*, 1–13.
- Dempsey, D. E., P. J. Langhorne, N. J. Robinson, M. J. M. Williams, T. G. Haskell, and R. D. Frew (2010), Observation and modeling of platelet ice fabric in McMurdo Sound, Antarctica, *J. Geophys. Res.*, *115*(C1), 1–16, doi:10.1029/2008JC005264.
- Dominé, F., R. Sparapani, A. Lanniello, and H. J. Beine (2004), The origin of sea salt in snow on Arctic sea ice and in coastal regions, *Atmos. Chem. Phys.*, *4*, 2259–2271.
- Dominé, F., A. S. Taillandier, W. R. Simpson, and K. Severin (2005), Specific surface area, density and microstructure of frost flowers, *Geophys. Res. Lett.*, *32*, L13502, doi:10.1029/2005GL023245.
- Eicken, H. (1992), Salinity profiles of Antarctic sea ice: Field data and model results, *J. Geophys. Res.*, *97*(C10), 15,545–15,557, doi:10.1029/92JC01588.
- Eicken, H. (1998), Factors determining microstructure, salinity and stable isotope composition of Antarctic sea ice: Deriving modes and rates of ice growth in the Weddell Sea, in *Antarctic Sea Ice Physical Processes, Interactions and Variability*, *Antarct. Res. Ser.*, vol. 74, edited by M. O. Jeffries, pp. 89–122, AGU, Washington, D. C.
- Eicken, H., H. Fischer, and P. Lemke (1994), Characteristics and distribution patterns of snow and meteoric ice in the Weddell Sea and their contribution to the mass balance of sea ice, *Ann. Geophys.*, *12*(1), 369–376.
- Elam, W. T., B. D. Ravel, and J. R. Sieber (2002), A new atomic database for X-ray spectroscopic calculations, *Radiat. Phys. Chem.*, *63*, 121–128.
- Frieß, U., J. Hollwedel, G. König-Langlo, T. Wagner, and U. Platt (2004), Dynamics and chemistry of tropospheric bromine explosion events in the Antarctic coastal region, *J. Geophys. Res.*, *109*, D06305, doi:10.1029/2003JD004133.

- Harrison, J. D., and W. A. Tiller (1963), Controlled freezing of water, in *Ice and Snow—Processes, Properties, and Applications*, edited by W. D. Kingery, pp. 215–225, MIT Press, Cambridge, Mass.
- Hutterli, M. A., T. Huthwelker, M. M. Miedaner, F. Enzmann, M. Ammann, M. Schneebeli, S. Maus, M. Stamanoni, A. E. Jones, and E. W. Wolff (2008), A 3D X-ray micro computer tomography perspective of sea ice, frost flowers and snow as sources of reactive halogens European Geophysical Union Spring Meeting, Vienna, April 13–18, 2008.
- Jeffries, M. O., W. F. Weeks, R. Shaw, and K. Morris (1993), Structural characteristics of congelation and platelet ice and their role in the development of Antarctic land-fast sea ice, *J. Glaciol.*, *39*(132), 223–238.
- Kreher, K., P. V. Johnston, S. W. Wood, B. Nardi, and U. Platt (1997), Ground-based measurements of tropospheric and stratospheric BrO at Arrival Heights, Antarctica, *Geophys. Res. Lett.*, *24*(23), 3021–3024, doi:10.1029/97GL02997.
- Lange, M. A. (1988), Basic properties of Antarctic sea ice as revealed by textural analysis of ice cores, *Ann. Glaciol.*, *10*, 95–101.
- Lannuzel, D., A. R. Bowie, P. C. van der Merwe, A. T. Townsend, and V. Schoemann (2011), Distribution of dissolved and particulate metals in Antarctic sea ice, *Mar. Chem.*, *124*(1–4), 134–146, doi:10.1016/j.marchem.2011.01.004.
- Lieb-Lappen, R., and R. W. Obbard (2012), Microstructural considerations of transporting sea ice samples from Polar Regions Abstract C43A-0579 presented at 2012 Fall Meeting, AGU, San Francisco, Calif., 6 Dec.
- Lieb-Lappen, R., and R. W. Obbard (2015), The role of blowing snow in the activation of bromine over first-year Antarctic sea ice, *Atmos. Chem. Phys. Discuss.*, *15*, 7537–7545, doi:10.5194/acp-15-7537-2015.
- Light, B., G. A. Maykut, and T. C. Grenfell (2003), Effects of temperature on the microstructure of first-year Arctic sea ice, *J. Geophys. Res.*, *108*(C2), 3051, doi:10.1029/2001JC000887.
- Marion, G. M., R. E. Farren, and A. J. Komrowski (1999), Alternative pathways for seawater freezing, *Cold Reg. Sci. Technol.*, *29*, 259–266.
- Martin, A., M. J. Anderson, C. Thom, S. K. Davy, and K. G. Ryan (2011), Response of sea-ice microbial communities to environmental disturbance: An in situ transplant experiment in the Antarctic, *Mar. Ecol. Prog. Ser.*, *424*, 25–37, doi:10.3354/meps08977.
- Massom, R. A., et al. (2001), Snow on Antarctic sea ice, *Rev. Geophys.*, *39*(3), 413–445, doi:10.1029/2000RG000085.
- Maus, S., T. Huthwelker, F. Enzmann, M. M. Miedaner, M. Stamanoni, F. Federica Marone, M. Hutterli, C. Hintermüller, and M. Kersten (2009), Synchrotron-based X-ray micro-tomography: Insights into Sea Ice Microstructure, *Rep. Ser. Geophys.*, vol. 61, edited by M. Leppäranta, pp. 28–45, Univ. of Helsinki, Helsinki.
- Notz, J., J. Wettlaufer, and M. G. Worster (2005), A non-destructive method for measuring the salinity and solid fraction of growing sea ice in situ, *J. Glaciol.*, *51*(172), 159–166.
- Obbard, R. W., H. K. Roscoe, E. W. Wolff, and H. M. Atkinson (2009), Frost flower surface area and chemistry as a function of salinity and temperature, *J. Geophys. Res.*, *114*, D20305, doi:10.1029/2009JD012481.
- Paige, R. A. (1966), Crystallographic studies of sea ice in McMurdo Sound, Antarctica U.S. Naval Civil Engineering Laboratory. Tech. Rep. R-494.
- Perovich, D. K., and J. A. Richter-Menge (1994), Surface characteristics of lead ice, *J. Geophys. Res.*, *99*, 16,341–16,350, doi:10.1029/94JC01194.
- Petrich, C., and H. Eicken (2009), Growth, structure and properties of sea ice, in *Sea Ice*, 2nd ed., edited by D. N. Thomas and G. S. Dieckmann, pp. 23–77, Wiley-Blackwell, Chichester, U. K.
- Prior, D., et al. (2015), Making EBSD on water ice routine, *J. Microsc.*, *259*(3), 237–256, doi:10.1111/jmi.12258.
- Rankin, A. M., E. W. Wolff, and S. Martin (2002), Frost flowers: Implications for tropospheric chemistry and ice core interpretation, *J. Geophys. Res.*, *107*, 4683–4695, doi:10.1029/2002JD002492.
- Robinson, N. J., M. J. M. Williams, C. L. Stevens, P. J. Langhorne, and T. G. Haskell (2014), Evolution of a supercooled ice shelf water plume with an actively growing subice platelet matrix, *J. Geophys. Res. Oceans*, *119*, 3425–3446, doi:10.1002/2013JC009399.
- Roscoe, H. K., K. Kreher, and U. Frieß (2001), Ozone loss episodes in the free Antarctic troposphere, suggesting a possible climate feedback, *Geophys. Res. Lett.*, *28*, 2911–2914, doi:10.1029/2000GL012583.
- Tang, T., and J. C. McConnell (1996), Autocatalytic release of bromine from Arctic snow pack during polar sunrise, *Geophys. Res. Lett.*, *23*(19), 2633–2636, doi:10.1029/96GL02572.
- Thomas, D. N., and G. S. Dieckmann (2009), *Sea Ice: An Introduction to its Physics, Chemistry, Biology and Geology*, 2nd ed., John Wiley and Sons West Sussex, U. K.
- Tison, J. L., D. Ronveaux, and R. D. Lorrain (1993), Low-salinity frazil ice generation at the base of a small Antarctic ice shelf, *Antarct. Sci.*, *5*(3), 309–322.
- Vogt, R., P. J. Crutzen, and R. Sander (1996), A mechanism for halogen release from sea-salt aerosol in the remote marine boundary layer, *Nature*, *383*, 327–330.
- Weeks, W. F., and S. F. Ackley (1982), *The Growth, Structure, and Properties of Sea Ice*, *CRREL Monogr.*, vol. 82-1, pp. 130, U.S. Army Cold Regions Research and Engineering Laboratory, Hanover, N. H.
- Wessel, S., A. Aoki, P. Winkler, R. Weller, A. Herber, H. Gernandt, and O. Schrems (1998), Tropospheric ozone depletion in polar regions: A comparison of observations in the Arctic and Antarctic, *Tellus, Ser. B*, *50*, 34–50.
- Yang, X., J. A. Pyle, and R. A. Cox (2008), Sea salt aerosol production and bromine release: Role of snow on sea ice, *Geophys. Res. Lett.*, *35*, L16815, doi:10.1029/2008GL034536.